

# Selenographic and Local Time Dependence of Lunar Exospheric Sodium as Observed by LADEE

E. C. M. Dawkins<sup>1,2</sup> , M. Sarantos<sup>1</sup> , D. Janches<sup>1</sup> , E. Mierkiewicz<sup>3</sup> , and A. Colaprete<sup>4</sup> 

<sup>1</sup> Heliophysics Science Division, NASA Goddard Space Flight Center, MD, USA; [erin.dawkins@nasa.gov](mailto:erin.dawkins@nasa.gov)

<sup>2</sup> Department of Physics, Catholic University of America, DC, USA

<sup>3</sup> Department of Physical Sciences and Center for Space and Atmospheric Research, Embry-Riddle Aeronautical University, FL, USA

<sup>4</sup> Space Science Division, NASA Ames Research Center, Moffett Field, Mountain View, CA, USA

Received 2021 October 4; revised 2022 July 12; accepted 2022 August 1; published 2022 September 21

## Abstract

Even though sodium (Na) has been known to be a constituent of the lunar exosphere for the past thirty years, limitations introduced by Earth-based observations make it difficult to determine how its distribution varies with local time. We used observations from the Ultraviolet and Visible Spectrometer instrument on board the NASA Lunar Atmosphere and Dust Environment Explorer mission to search for evidence of near-instantaneous dayside variation of exospheric Na across one lunation (2014 February–March). Through comparison with model simulations, the data appear to be consistent with persistent southern enhancements of Na, while no evidence of systematic depletion of the Na exosphere reservoir within two hours of local noon was obtained. The results indicate an enhancement of the gas density over Mare regions and the lunar nearside; though this finding could mean that the weak Na emission is lost in the scattering continuum over brighter soils. Day-to-day variability is observed and may reflect a changing solar wind and meteoroid environment combined with inhomogeneities in the gas–surface interaction parameters and Na distribution on the lunar surface. We found that, due to the limited viewing geometry and sensitivity of the instrument to scattering from the bright lunar surface, it is difficult to uniquely separate the latitudinal and local time variations of Na.

Unified Astronomy Thesaurus concepts: [Lunar composition \(948\)](#); [Lunar atmosphere \(947\)](#); [Exosphere \(499\)](#)

## 1. Introduction

Despite being a trace constituent of the thin lunar exosphere, sodium (Na) is readily observed remotely due to its strong resonance emission at 589 nm and is an important tracer of processes that produce collisionless exospheres throughout the solar system. Observations from Earth have provided insight into the altitude and latitude dependence of exospheric Na (e.g., Potter & Morgan 1988a, 1988b; Tyler et al. 1988; Sprague et al. 1992; Potter & Morgan 1998; Potter et al. 2000; Kagitani et al. 2010; Colaprete et al. 2016; Killen et al. 2019, 2021 and references therein). A cold component to the Na exosphere was identified by Sprague et al. (1992) as well as Potter & Morgan (1998), who derived an atmospheric scale height of  $120 \pm 42$  km. Subsequent studies found that the Na exosphere also contains nonthermal components that may extend out to nine lunar radii or more (e.g. Flynn & Mendillo 1993; Mendillo & Baumgardner 1995), with broader scale heights of  $\sim 1000$  km (e.g., Kuruppuaratchi et al. 2018; Killen et al. 2019, 2021). Latitudinal dependencies were imaged most recently with the coronagraphic measurements by Killen et al. (2019). The exospheric Na source is predominantly attributed to photon-stimulated desorption (PSD) of surficial Na by solar photons, with additional contributions due to bombardment of the lunar surface by meteoroids and the solar wind (e.g., Flynn & Mendillo 1993; Mendillo & Baumgardner 1995; Stern 1999; Yakshinskiy & Madey 1999; Kagitani et al. 2009; Sarantos et al. 2010; Colaprete et al. 2016).

On 2013 September 7, the LADEE spacecraft (Elphic et al. 2015) embarked on a 223 days lunar mission, which ended on

2014 April 18. The science phase of the mission was conducted in a near-equatorial (inclination of  $157^\circ$ ), retrograde, near-circular orbit. The Ultraviolet and Visible Spectrometer (UVS), one of three instruments on board this mission, measured the light scattered from the lunar exosphere and surface across a wavelength range of 230–810 nm with a spectral resolution  $< 1$  nm, and a dispersion (number of nanometers per pixel) of  $\sim 0.6$  nm (Colaprete et al. 2014). For five lunations, LADEE/UVS obtained the first near-continuous measurements of Na and K in the lunar exosphere within  $15^\circ$  of local noon, which were analyzed by Colaprete et al. (2016). The Na and K abundances were found to vary with lunar phase; K following its distribution on the surface while Na showed a similar factor of two increase in abundances over the subsolar point near full moon phases. Surface enhancements (Athiray et al. 2014) or solar wind effects have been considered as the reasons behind this Na variation. Knowledge of column densities at other local times could help differentiate between these factors.

While previous work has characterized the latitudinal and altitudinal dependence of exospheric Na, as well as the temporal variation above local noon, there is only a limited understanding of the spatial variation in local time. This is due to the fact that it would take two weeks for Earth-based observations to cover all dayside local times, thereby convolving the spatial and temporal effects. In this work, we expand the analysis of LADEE/UVS data by Colaprete et al. (2016) to derive variations of exospheric Na across an expanded portion of the lunar sunlit hemisphere for one lunation. The observed Na variation with local time is presented, in conjunction with lunar exosphere model simulations, to explore the implications that these local time and lunar phase variations have on the source and sink processes that are important to the lunar exosphere.



Original content from this work may be used under the terms of the [Creative Commons Attribution 4.0 licence](#). Any further distribution of this work must maintain attribution to the author(s) and the title of the work, journal citation and DOI.

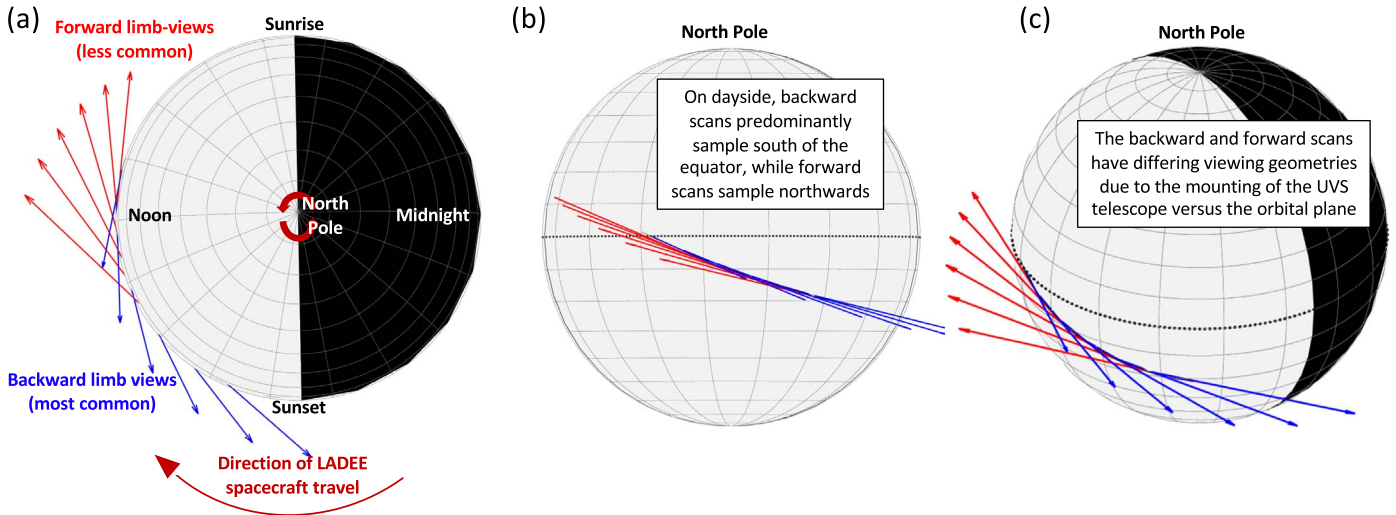


**Figure 1.** (a) Schematic of LADEE/UVS viewing geometry, which shows the two different limb-viewing angles. (b)–(c) North–south viewing geometry for lines sampled during one day of observations.

## 2. Data Reduction

### 2.1. Data Set

In this work, we used UVS spectra made at two second (2 s) time integrations, using all dayside limb scans for 2014 February–March. This one month period was selected as it was bounded by two *dark* count (thermal current) calibration measurements with a low background. Because the LADEE mission had limited pointing capabilities, the majority of the 2 s measurements were made during backward-viewing limb scans with the instrument pointing in the antiram direction and southward (see Figure 1). In addition, the majority of measurements were obtained at telescope grazing point altitudes of  $\sim$ 40 km, although this varied during periods when the instrument was performing exospheric nods near sunset (not shown in Figure 1). During this mid-February to mid-March timeframe, there were thirteen days in which the forward-viewing limb measurements were made, in addition to the backward views. In order to extract the Na emission, a significant number of processing steps were performed, including preprocessing of the raw UVS spectra to subtract the instrument effects and cosmic ray contamination, binning of the individual spectra to improve signal-to-noise ratio (S/N), correction for white light scattering (*infilling*), and accounting for wavelength shifts. Each of these steps will subsequently be described in detail.

### 2.2. Preprocessing of the Raw UVS Spectra

Instrument bias, cosmic rays, and second-order grating effects were removed from the raw spectra. Voltage bias, a nonuniform offset from zero across the CCD, was subtracted by forming a running mean of the four bevel pixels on the right of the CCD array (Colaprete et al. 2014; Wooden et al. 2016). To identify cosmic ray impacts in the continuously varying continuum of the sunlit hemisphere, we combined the measurements from a given pixel across each 20 minutes UVS activity and fit a smooth curve with a Savitzky–Golay function (Savitzky & Golay 1964). This filtered out large cosmic rays with  $3\sigma$  clipping on a pixel-by-pixel basis. The second-order grating effects at wavelengths exceeding 500 nm were subtracted using the second-order function described

in Colaprete et al. (2014; available at [https://atmos.nmsu.edu/PDS/data/PDS4/LADEE/uvb\\_bundle/calibration/radiance.tab](https://atmos.nmsu.edu/PDS/data/PDS4/LADEE/uvb_bundle/calibration/radiance.tab)).

Dark counts as a function of time and sensor temperature were estimated and removed. Dark calibration measurements were typically performed once per month at full moon throughout the LADEE mission lifetime. Because the expected exospheric Na brightness is small (<20 digital counts, or DN, compared to the spectrum continuum of 100–1000 s of counts), and a 1 kR excess corresponds to  $\sim$ 1.5 DN/2 s, it is vital that the dark measurements (0.5–1 DN in 2 s near the Na pixels) and their change with time be correctly characterized and subtracted from the spectra. For this we used UVS limb measurements obtained when the spacecraft was between  $30^\circ$  inside the Moon's shadow and local midnight, and for each pixel we fit a two-dimensional thin spline to UVS nightside measurements throughout the period of study. Smoothed with this method, the measurements obtained near full moon gave estimates that were found to be consistent with dark calibration activities (example presented in Figure 2). Finally after these careful preprocessing steps, the scrubbed individual spectra were converted from photon counts to radiances using the UVS instrument calibration function ([https://atmos.nmsu.edu/PDS/data/PDS4/LADEE/uvb\\_bundle/calibration/radiance.tab](https://atmos.nmsu.edu/PDS/data/PDS4/LADEE/uvb_bundle/calibration/radiance.tab)).

### 2.3. Additional Processing Steps: Accounting for Wavelength Shifts, Choice of Solar Reference Spectra, and Removal of White Light Scattering

Besides using the instrument wavelength calibration (Colaprete et al. 2014), we found that wavelength shifts (mean = 0.53 nm, SD = 0.11 nm) occurred during a sequence, likely as a result of changes in the reflectance slopes when the spacecraft moved across local times and different soils. These wavelength shifts alter the apparent depths of the Fraunhofer lines and can be misattributed as exospheric emission if not accounted for. As part of the general processing, the individual spectra were detrended (*continuum removed*) by dividing with a linear fit of the continuum background from adjacent pixels on either side of the Na feature (approximately 585.4–587.7 and 591.1–594.4 nm). This detrending partially—but not fully—removed the impact on wavelength of changes in reflectance

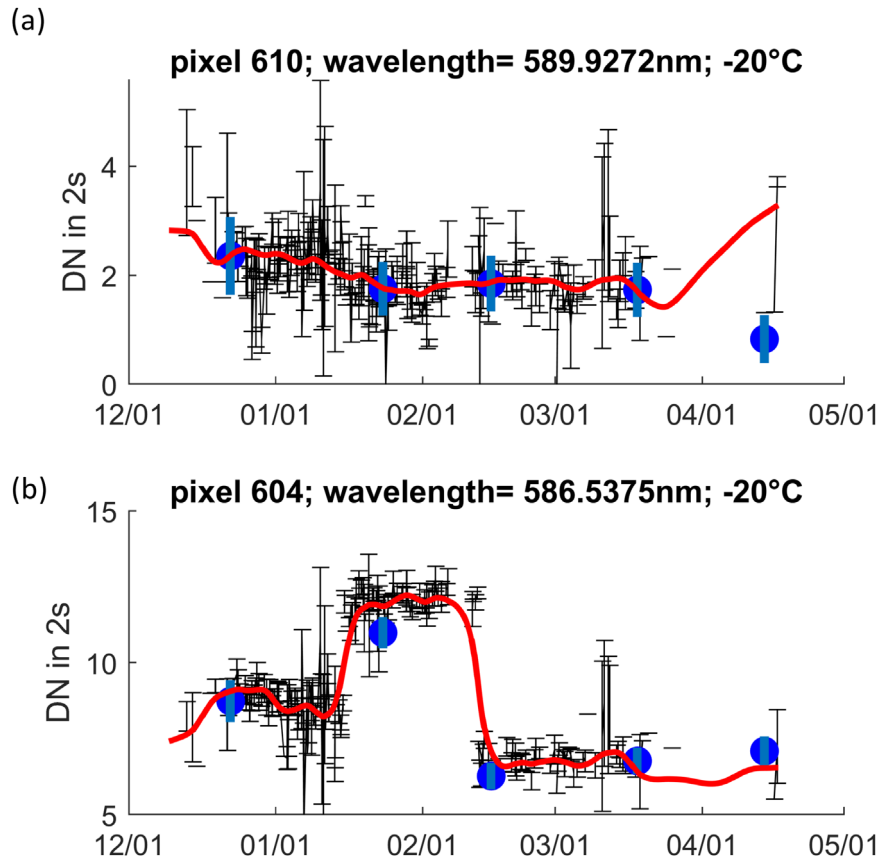


**Figure 2.** Estimation of dark counts from the UVS nightside data, for a Na wavelength pixel (panel (a), pixel 610,  $\sim 589.93$  nm) and a nearby *hot wing* pixel (panel (b), pixel 604,  $\sim 586.54$  nm). The filled circles indicate UVS dark calibration measurements, while the black error bars correspond to the nightside measurements per activity. The red curve corresponds to a temperature- and time-dependent thin spline fit to UVS nightside data (here corresponding to  $-20^{\circ}\text{C}$ ). The thin spline closely follows that of the UVS dark calibrations and can thus be used as a proxy for time-dependent darks. Compared to other lunations, the nightside data and UVS dark calibrations exhibited very little variation during the mid-February to mid-March lunation period, hence the choice of this initial study period in this work.

slope (e.g., Clark & Roush 1984). To mitigate this, a fine spline was fit to each continuum-removed spectrum and used to determine the minimum of a Fraunhofer feature and identify the wavelength offsets relative to a reference point (i.e., the center point between the Na D-lines). The characterization of this wavelength shift for each measurement is important as it determines which solar reference spectrum to later use for differencing, as well as for calculating the infilling correction.

Because the fixed point noise (systematic cross-pixel variation) of the CCD was found to be comparable to the signal we were trying to estimate, we did not use a convolved theoretical solar spectrum as solar reference. To account for the fixed point noise in our differencing, we compiled a library of solar reference spectra (*masks*), produced for each detected wavelength shift, by combining the deepest spectra observed over this month, which were assumed to be devoid of emission and uncontaminated by any scattering inside the telescope. These spectra were found to exhibit much deeper Fraunhofer lines than the spectra obtained during solar and/or surface calibration activities. Along with possible contamination by off-axis scattering, another reason to not use the solar calibration spectra as reference spectra is that they were obtained early in the mission—months before these 2014 February–March measurements—and thus before pixels started aging. For this library, all individual spectra described in Section 2.4 were divided into groups depending on the wavelength shifts detected, and a mask was formed for each

group from the median of the lowest 5% deepest spectra. Each of these masks exhibited different line shapes and sigma widths specific to the wavelength shift. We found that the sigma widths used were typically smaller than the sigma used in the UVS instrument function ( $\sim 0.6$  at 589 nm, Figure 7 of Colaprete et al. 2014) likely as the lines have higher spectral contrast due to off-axis instrument scattering. Prior to differencing, a specific mask can be selected from this library, which corresponds to the wavelength shift detected in any given measured spectrum. The total Na emission is derived by integrating across the theoretical Na line shape accounting for any wavelength offsets and using a sigma width consistent with that of the solar mask.

Finally, it was observed that, even after accounting for these wavelength offsets, the band depth of not only Na but also many Fraunhofer features in the UVS visual wavelengths—devoid of exospheric lines—tended to change as a function of local time and/or continuum level (Figure 3). This change in band depth, likely due to off-axis light scattering onto the CCD, causes apparent *infilling* of many solar Fraunhofer features. Without careful characterization and subtraction, this offset background would be misinterpreted as additional Na emission. To quantify this correction using measured spectra, four nearby Fraunhofer lines (centered at  $\sim 602$ ,  $\sim 616$ ,  $\sim 650$ , and  $\sim 672$  nm, each with no known exospheric emission) were used to estimate the infilling as a function of wavelength shift. Libraries of solar masks were formed for each of these

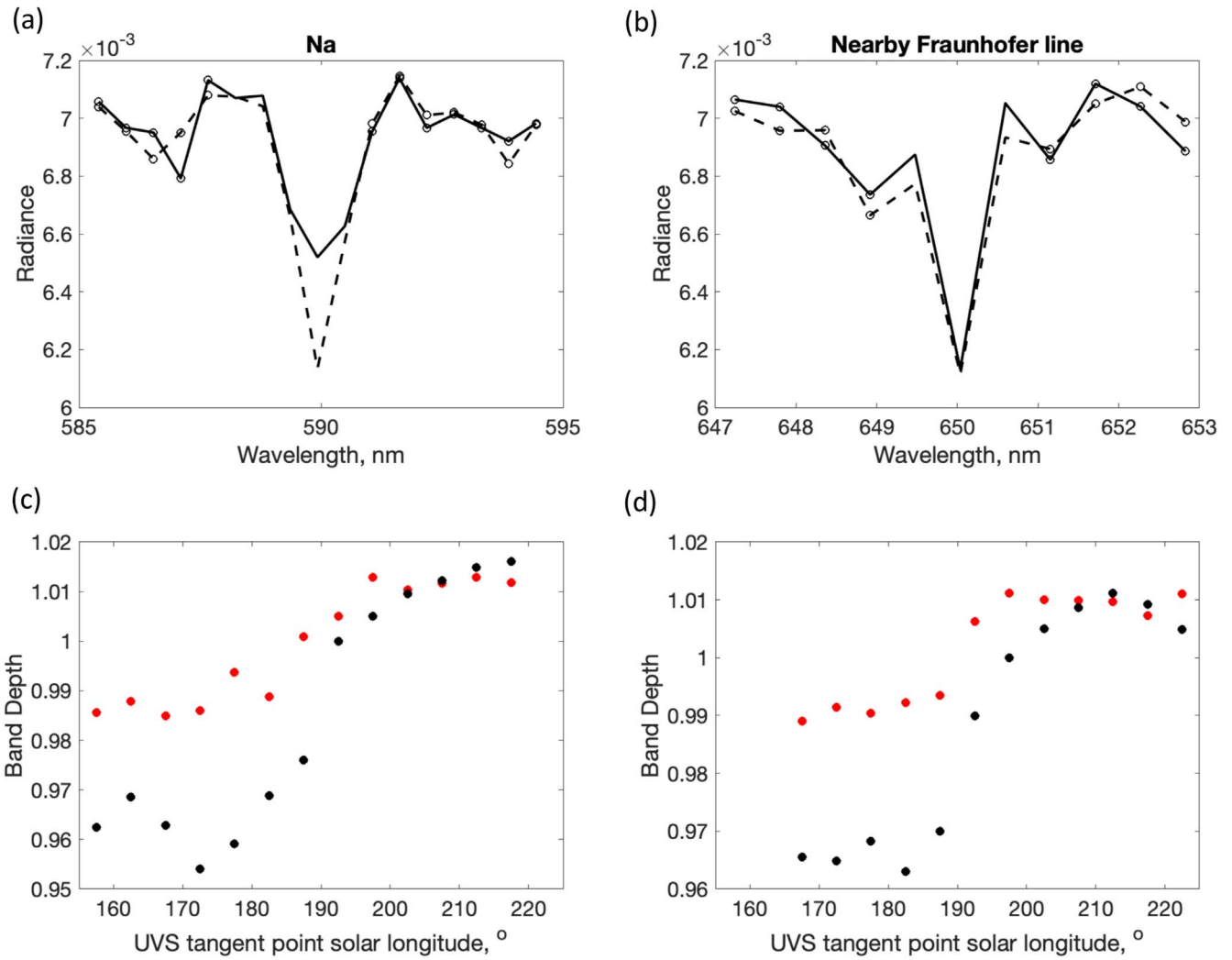


**Figure 3.** Infilling is observed at different wavelengths, even those where no exospheric lines are expected, and must be removed before extracting the Na emission. Panels (a) and (b) show example measured (solid line) with the corresponding solar mask (dashed lines) for a specific day and local time, for Na and a nearby Fraunhofer line while panels (c) and (d) show the relative band depth changes of Na (red circles) and a nearby Fraunhofer line (black circles) for two different days, as a function of UVS tangent point solar longitude. Band depth (BD) is defined as the ratio between the line center and the wings (indicated by open circles in panels (a) and (b)). All band depths have been normalized with respect to the median band depth for Na or the Fraunhofer line, respectively. One can see that at the subsolar point—where solar longitude  $\sim 180^\circ$ —Na has a shallower BD than can be explained by infilling alone, indicating Na emission. In the prenoon sector (solar longitude  $> 200^\circ$ ), there is no discernible difference between the relative band depths of either Na or the Fraunhofer line, which suggest that any variation in the BD here is predominantly due to infilling associated with changes in reflectance.

absorption lines and were used to estimate the infilling of each spectrum at the relevant wavelengths. Finally, a set of random forest models (i.e., nonparametric corrections) was produced using the following as inputs: the wavelength ( $\lambda$ ) of each of these four Fraunhofer lines, their  $\lambda/2$  value (to account for any mismatches in second-order correction mapping), the global slope between 580 and 680 nm (to account for changes in reflectance), the continuum level, and relative band depth of the solar mask, all as a function of wavelength offset. Trained with the individual spectra from each of these lines, these random forest models were used to determine the infilling that must be subtracted from each Na spectrum prior to differencing with the solar mask. The resulting excess, if any, from a solar reference spectrum of the appropriate wavelength offset was considered to be indicative of Na emission.

We used the UVS surface calibration spectra, which were made toward the end of the LADEE mission (in 2014 April), to evaluate the infilling correction technique (Figure 4.). These surface calibration spectra had a very short integration time

(150 ms), and as such, they are assumed to be free of Na emission, as well as cosmic ray hits. Thus, despite these measurements being taken under a different geometry than the limb scans, these spectra offer an excellent opportunity to test whether the infilling correction technique can be used to remove white light scattering at 589 nm. In theory, after accounting for wavelength shifts, the only difference between the band depths of the measured and library spectra would be due to changes in reflectance. A perfect correction would therefore result in identical band depths of the post-corrected measured and library solar mask spectra at  $\sim 589$  nm. In the pre-correction (Figure 4, panel (a)), one can see that both the measurements at  $\sim 589$  nm and the nearby Fraunhofer line have an underlying variation with respect to local time, with both demonstrating a 0.15%–0.4% difference between the pre-corrected and mask band depths. In the post-correction (panel (b)), this underlying variation in the Fraunhofer line has been removed, such that the differences between the post-corrected and mask band depths are near zero (within  $\pm 0.02\%$ ).

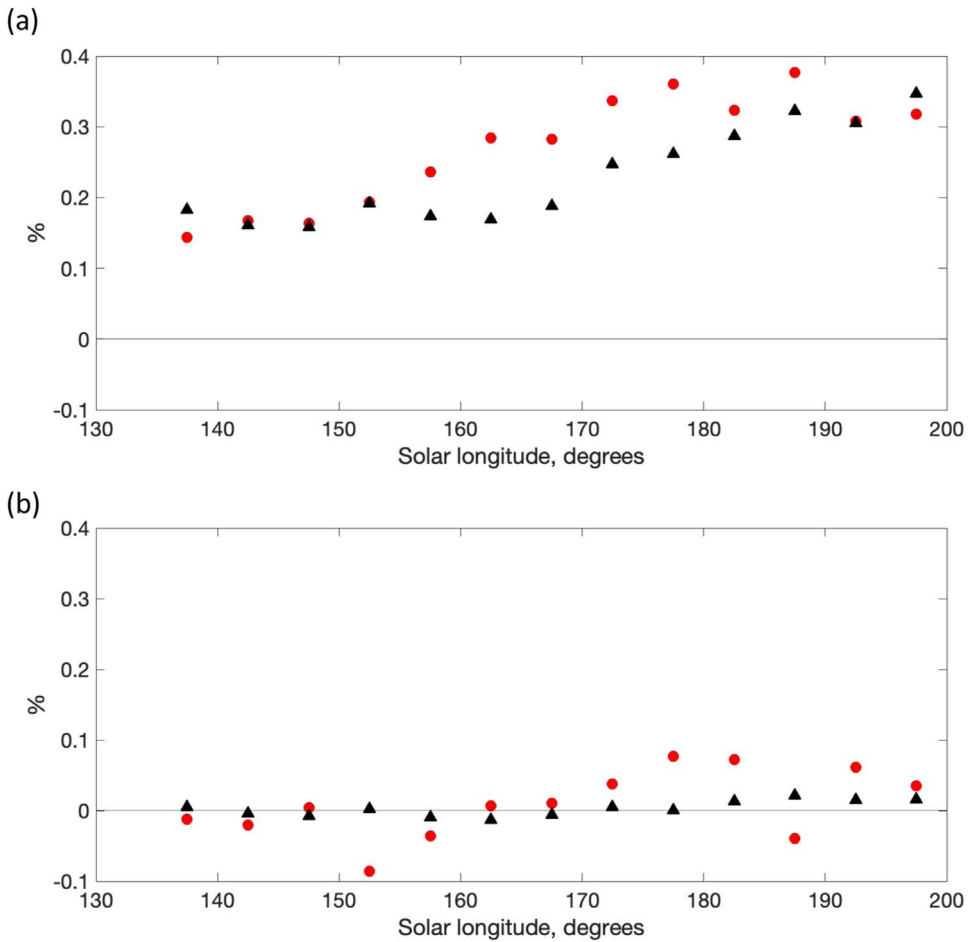


**Figure 4.** The infilling correction routine is capable of removing the underlying variation due to changes in reflectance across local times. Here we present a case study for a surface calibration measurement made on 2014 April 16, which shows the variation of the measured band depth relative to the respective mask for both Na (red filled circles) and a nearby Fraunhofer line ( $\sim 603$  nm, black filled triangles), pre-correction and post-correction for infilling. All points represent the geometric mean for the given local time. Panel (a) depicts the percentage change in band depth of the initial (pre-corrected) measurement relative to the solar mask, with the red filled circles showing the percentage change in band depth for Na wavelengths. Panel (b) shows the percentage change in band depth of the post-corrected measurement relative to the solar mask for both Na (red) and Fraunhofer line (black) data.

Similarly, one can see that, after applying the infilling correction as predicted by the random forest model, the underlying variation at  $\sim 589$  is also greatly reduced, such that the difference between the post-corrected and mask band depths is now well within  $\pm 0.1\%$  (and largely within  $\pm 0.03\%$  for the majority of local times). Therefore, although not a perfect correction, this proof of concept demonstrates that the infilling correction trained on independent Fraunhofer lines is capable of removing the infilling at another nearby line (in this case,  $\sim 589$  nm).

#### 2.4. Extracting Na Emission

After preprocessing, the individual spectra were binned into 24 hr periods and  $5^\circ$  local time bins determined by the solar longitude of the telescope grazing point on the lunar dayside between  $90^\circ$  and  $270^\circ$ . The resulting spectra were subsequently differenced with a solar reference spectrum continuum (*mask*) in order to determine the exospheric Na signature. An illustration of the exospheric Na extraction process is also shown in Figure 5. Finally, the geometric mean was formed for each local time bin; this coadding step is particularly important at local times on either side of the subsolar point, where

exospheric emissions may be weaker with reduced signal-to-noise.

#### 2.5. Estimating Uncertainties and Quality Control

Uncertainties in the total Na emission include the uncertainties associated with the estimation of time-dependent darks, bias subtraction, infilling correction, cross-pixel variation, least-square fitting error, and readout noise, and those in the fitting and correction of the solar masks. Bootstrapping (repeated sampling with replacement) is performed on the local time binned individual spectra prior to forming the geometric means and subsequent full processing, in order to derive an estimate of the bootstrapped error on the derived total Na emission values. An additional analysis derived the uncertainties associated with the wavelength shifts and subsequent solar mask correction. All reported vertical uncertainties consist of the bootstrapped errors, standard error of the median, mask correction uncertainties, and systematic uncertainties due to dark count and radiometric calibration uncertainties, all added in quadrature.

Due to the weak Na S/N, careful quality control is vital in order to avoid false positives when differencing. To mitigate against this, we coadd data, perform the preprocessing steps

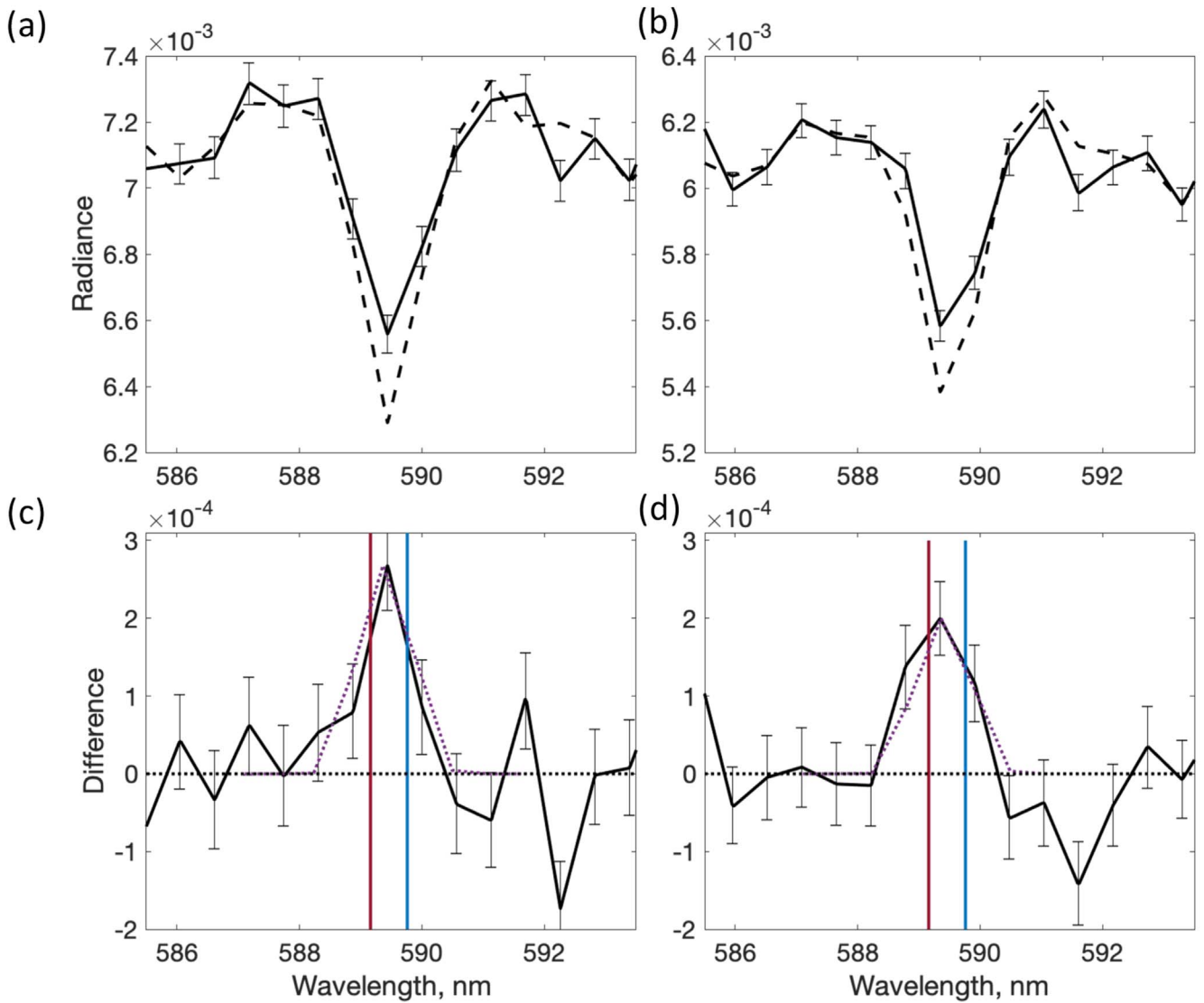


**Figure 5.** Example spectra to illustrate the extraction of exospheric Na. Top panels (a) and (b) show the processed measured spectra (black solid line) for two different examples, with a corrected solar reference spectrum (dashed line) scaled to the same wing continuum levels (between approximately 585.4–587.7 and 591.1–594.4 nm). The bottom panels (c) and (d) show the resulting respective differences after subtracting the scaled solar spectrum from the measured spectra. Vertical lines indicate the Na D<sub>1</sub> and D<sub>2</sub> emission lines. The purple dotted line is the theoretical convolution of the D<sub>1</sub> and D<sub>2</sub> lines using a sigma width derived from the solar mask. Units:  $\mu\text{W cm}^{-2} \text{nm}^{-1} \text{sr}^{-1}$ .

described in Section 2.2, in addition to the removal of individual spectra with low (<250) or very high counts in order to improve the S/N, and to prevent possible CCD nonlinearities at lower counts affecting the results. Finally, after differencing, we only consider the differenced spectra where the root mean square error (RMSE) of the Na signal pixels exceeds the RMSE of the wing pixels.

### 3. Results and Discussion

#### 3.1. Constraints on Exospheric Structure

Because the local time coverage is incomplete from the daily data, Figure 6 shows a composite local time distribution of exospheric Na across the 2014 February–March lunation. Each box contains an average of 3500 individual daily excess spectra. Excess emission is plotted as a function of the local time of the tangent point of each sightline, binned every 5°. The box-and-whisker plot indicates the median Na emission, along with the range and upper and lower quartiles at the center of

each 5° local time bin. The median tangent heights of all the included measurements are 42.06 km ( $\pm 2.59$  km) for backward views and 40.21 km ( $\pm 3.13$  km) for forward views. Although it is apparent that there is considerable variation of Na intensity at each local time over this month, a repeatable trend with local time is demonstrated in Figure 7, where a selection of evenly spaced daily variations are highlighted. The former figure combines the spatial and temporal variability, while the latter shows the spatial variability, albeit with a large uncertainty because of the low S/N. An illustration of the differences in the local time variation with and without infilling correction, discussed in Section 2.3, is presented in Figure 8.

The range of Na emission values observed by LADEE/UVS is consistent with ground-based measurements reported in Sprague et al. (2012), Sarantos et al. (2010), and Killen et al. (2019), and references therein. Due to the limited number of days on which forward-viewing scans (shown in red) were performed, it should be noted that the forward-viewing data set represents a subset (13 days) of the backward-viewing data set

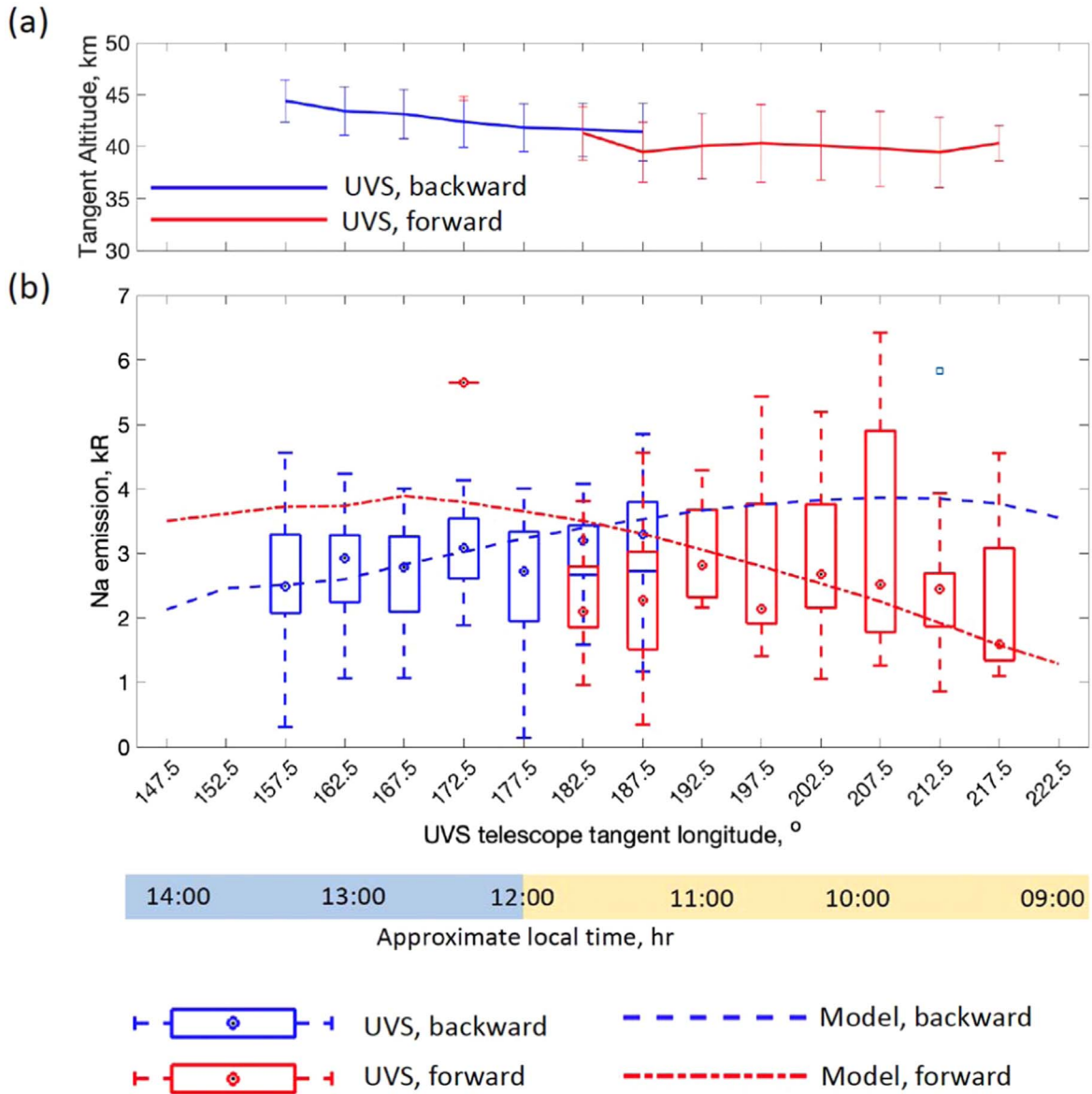


**Figure 6.** Total Na emission (units: kR) as a function of UVS telescope tangent longitude (and approximate local time) for the 2014 February–March lunation for all backward (blue) and forward (red) viewing limb measurements. The box-and-whisker plot shown in panel (b) indicates the median Na emission, along with the range and upper and lower quartiles at the center of each 5° local time bin. The box and vertical *whisker* lines represent variability rather than errors. The self-colored dashed and dotted-dashed lines correspond to centered atmosphere models with source distributions of  $F_{\text{SZA}} \propto \cos(\text{SZA})$  and high speeds, and a temperature-dependent sticking probability, for backward- and forward-viewing geometries, respectively. The median tangent altitude for each of the views is shown in panel (a), with  $\pm 1$  standard deviation represented by the vertical bars.

(shown in blue). Nevertheless, both viewing geometries result in similar distributions with local time, showing weak enhancements near the subsolar point, which are offset depending on viewing angle. The afternoon and near sunset local times are more likely to be contaminated by infilling because of the altitude probed. This region, where many measurements were filtered out due to the  $\text{RMSE}_{\text{Na}} > \text{RMSE}_{\text{wings}}$  requirement (see Section 2.5) is the most sensitive to the infilling correction technique described in Section 2.3.

We contrasted simulated and observed data to understand the effect of the UVS viewing geometry, such as changing altitude and local time of observations. Simulation results are presented in Figure 6 (blue dashed and red dotted-dashed lines for backward and forward-viewing geometries, respectively), as well as in following Figures 7–11. Particle trajectories were tracked using the Monte Carlo model presented in Collier et al. (2014) and

Bennett et al. (2016). These simulations assumed an initial temperature range of  $T = 1200\text{--}4000$  K. It should be stressed that the limited viewing geometry of LADEE and the inability to perform systematic altitude scans do not permit us to directly assess the source temperature. The high temperature assumed here is taken from ground-based coronagraphic measurements (Killen et al. 2019, 2021) and is presumed to arise from nonthermal speed distributions for PSD, impacts, and sputtering. The low end ( $T = 1200$  K) is considered to be the core of the PSD speed distribution (Kurupparatchi et al. 2018; Sarantos et al. 2010). When test particles met the lunar surface, a sticking coefficient,  $s$ , was utilized to consider the trapping by the soil. The two versions tested were as follows: (1)  $s = 1$  for all surface locations, or (2) a temperature-dependent sticking coefficient (LeBlanc & Johnson 2003) and full energy accommodation to the surface temperature at the reimpact site. When a particle was determined to

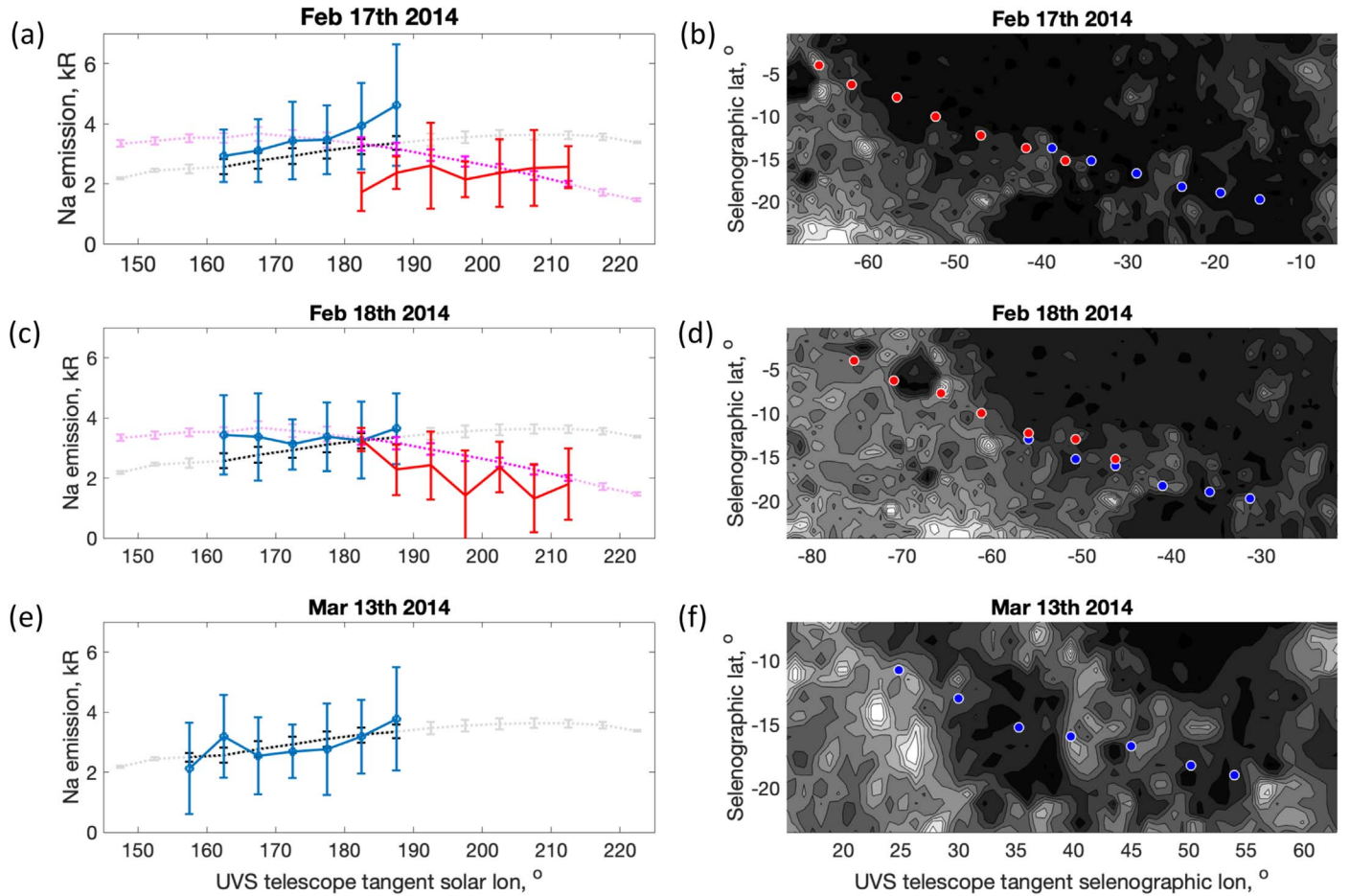


**Figure 7.** Examples of daily derived Na variation as a function of local time for three individual days (panels (a), (c), (e)). Backward limb measurements are shown in blue while forward limb views, where available, are in red. The vertical bars represent  $\pm 1$  standard deviation. The corresponding backward and forward model views are shown in black and magenta, respectively (these lines are intentionally faded for local times in which no UVS measurements are available). Panels (b), (d), (f) show the selenographic latitude and longitude of the UVS telescope tangent point and underlying lunar surface for each of the days, respectively.

stick to the surface, no subsequent desorption events were considered. It has been suggested that  $\sim 60\%$  of Na atoms that stick to the lunar regolith are lost to microscopic shadows on each bounce (Sarantos & Tsavachidis 2020). The model assumed that the Na source rate near the subsolar point is  $\sim 2 \times 10^6$  Na atoms  $\text{cm}^{-2} \text{s}^{-1}$  (Sarantos et al. 2010).

The spatial distribution of the simulated Na source was varied. Because the LADEE spacecraft is drifting both in local time as well as latitude (Figure 1), and coronagraphic observations indicate a latitudinal variation of the Na exosphere, it is important to understand whether latitudinal variations mask the variations with local time. Using guidance from the coronagraphic measurements of Killen et al. (2019, 2021), six types of spatial distributions were simulated: (1) a source having both north and south midlatitude enhancements with an equatorial depletion; (2) a source rate distribution with a north enhancement; (3) a source with enhancement in the south; (4) a centered atmosphere with the flux decreasing from local noon, but elongated in latitude (thus, noted as “elongated cosine” in the figure legends) to account for the finding that due to the transport of adsorbates from equatorial regions to the poles, the column abundance decreases more slowly than the cosine of latitude (Killen et al. 2021); (5) a case like (4) but with a peak shifted  $20^\circ$  toward dawn to test a hypothetical depletion of the Na adsorbate reservoir near noon (e.g., Yokota et al. 2014); and finally (6) as in (5) but with a peak shifted  $20^\circ$  toward dusk. Only the last three models have a dependence on

local time if  $s = 1$ , whereas the temperature-dependent sticking introduces a local time dependence to all models as Na sticks more rarely at the highest noon temperatures. While coronagraphic measurements are likely insensitive to accommodated atoms because they probe altitudes exceeding 150 km (Killen et al. 2019, 2021), LADEE/UVS is potentially sensitive to them. The global distributions resulting from some of these assumed models can be visualized in Figure 9.

Through these models, we run the LADEE geometry as it evolved day by day. The resulting comparisons of LADEE data with the assumed models are presented in Figures 10 and 11. One of the metrics for this model-data comparison is the rate of change (slope) of brightness with local time. As a rule, the elongated cosine models have steeper slopes with local time than the remaining models, which have limited to no dependence on local time. An additional metric is the local time at which the data from the two viewpoints meet (around noon). Generally, models with a northern enhancement and/or accommodation shift this point downwards of the subsolar point when accounting for the LADEE viewing.

The LADEE data are sensitive to north–south asymmetries due to the differences in UVS sampling geometry: backward scans point southward along the inclined LADEE orbital plane, whereas forward scans point northward along the orbital plane (see Figure 1). Although they correspond to different local times, the slightly enhanced Na in the backward versus the

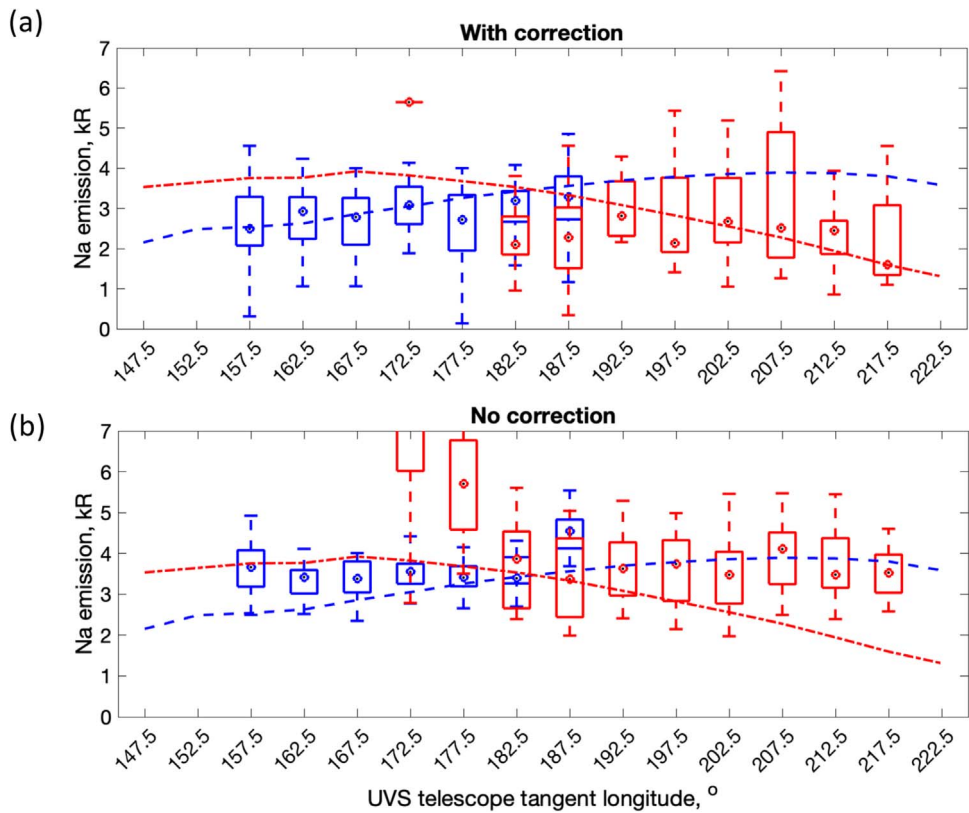


**Figure 8.** Illustrating the effect of correcting for infilling. Panel (a) reproduces the data shown in Figure 6 in the main manuscript and depicts the Na local time variation after infilling has been subtracted. Panel (b) shows this same data set but with no correction made for infilling. Without correction, this infilling is interpreted as additional Na variation, and one can clearly see the effect of this on the post-noon side, as well as resulting in inflated Na emission values across all local times. It should be pointed out that panel (b) contains data with better local time coverage. This is due to a quality control filtering criterion in which data are only included for a given day and local time if the root mean square error of the Na signal region exceeds that of the wing regions.

forward scans could indicate a north–south asymmetry as occasionally seen from Earth-based observations (Potter & Morgan 1991; Killen et al. 2019). For all temperatures and accommodation scenarios, we can exclude the possibility of persistent northern enhancements as, according to our models, the crossing point of the backward and forward views should be dawnside rather than near the subsolar point as seen in the UVS data (see Figure 11). The data could instead indicate enhancements in the south. Based on the chi-squared value fit, of all models tested, the best fit was provided by the  $T = 4000$  K model with a southern enhancement in source rate and with complete sticking (Figure 11, panel (f), dashed line). The next best fit was provided by the  $T = 4000$  K model with a midlatitude enhancement and equatorial depletion with complete sticking (Figure 11, panel (a), dashed line). For all models, those with complete sticking are consistently in closer agreement with the UVS data than those with temperature-dependent sticking and full thermal accommodation of rebounded particles, which corroborates the conclusions of low accommodation of Na onto Mercury’s surface (e.g., Wang & Ip 2011).

The data, viewed with this superposed-epoch analysis (Figures 6–11), fail to identify dawn–dusk asymmetries. A dawn–dusk asymmetry in local time variation could result from nighttime buildup of adsorbed or condensed Na gas-phase atoms onto lunar soils, leading to a progressive release of gases from the terminator toward noon. Additionally, such an asymmetry might reflect the presence of a predominantly dawnside meteor impact source (Janches et al. 2018;

Pokorný et al. 2019). A small offset of the Na peak by  $\sim 10^\circ$  prenoon was inferred from a similar superposed-epoch analysis of Na ion measurements (Yokota et al. 2014). Similarly, Killen et al. (2021) noted with coronagraphic measurements the enhancements of the column density at off-noon local times; though the possibility of systematic selenographic variation was not considered. While due to the increased scattering, data are available only at a limited range of local time coverages (i.e., no processed measurements prior to  $\sim 09:30$  LT); there is no evidence of any dawn–dusk asymmetry in the Na exosphere sampled by UVS within two hours of noon. Both the slopes and offset of relevant models (5) and (6) do not match the combined forward and backward data (Figure 10, panels (c) and (d)).

To summarize the findings of this section, we offer two conclusions. First, there is evidence of north–south asymmetry, with persistent enhancements of Na emission from the southern hemisphere as the best explanation of the observed data. This introduces some uncertainty about whether the LADEE/UVS trend can be solely attributed to local time. And second, there is no evidence of depletion of the Na exosphere within hours of local noon as the shifted models are poor fits.

### 3.2. Temporal and Selenographic Variability

Figure 12 presents the temporal variation of Na emission across the studied lunation period, for a selection of local time bins;  $\sim 11:30$  LT,  $\sim 11:45$  LT,  $\sim 12:15$  LT, and  $\sim 12:45$  LT. Data consist of backward-viewing limb measurements only,

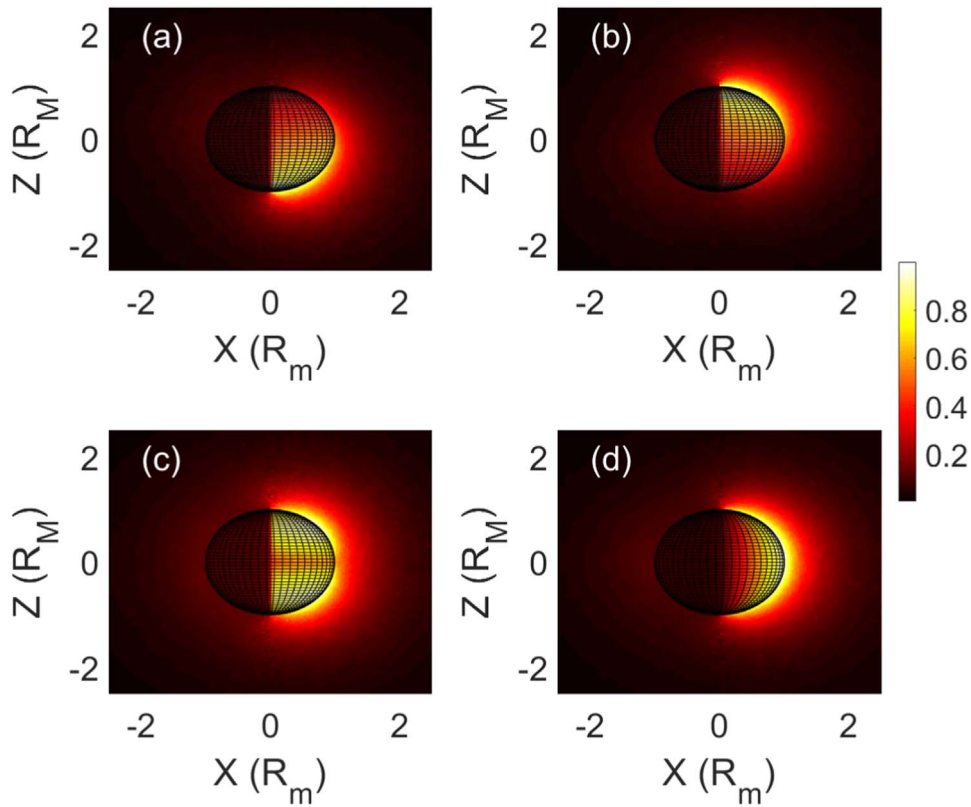


**Figure 9.** Illustration of different model source distributions that were compared to LADEE data. Following results from coronagraphic measurements (Killen et al. 2019, 2021), we tested: (a) a source with enhancement in the south, (b) a source with enhancement in the north, (c) a source having both north and south midlatitude enhancements with an equatorial depletion, and (d) a centered atmosphere with source flux,  $F$ , decreasing from the subsolar point as  $F \propto \cos(\text{solar longitude}) * \cos^{1/8}(\text{latitude})$ . The color indicates relative density (in arbitrary units) in the north–south plane through local noon, as well as the near-surface density at all prenoon local times.

and both the Na emission (markers colored by selenographic longitude) and column abundance are presented (gray diamonds, right-hand-side  $y$ -axes). Column abundance was estimated from emission by dividing with the g-value Killen et al. (2019) for atoms at rest with respect to the Moon at the time of the observation. Full moon and new moon phases are indicated (red and gray arrows, respectively), in addition to periods in which the Moon is either within the concentrated plasma of the Earth’s magnetosheath (green shaded) or within the magnetotail region (orange shaded) and thus shielded from the solar wind. The black solid curves represent a second-order polynomial fit to the UVS emission data, while the light gray line represents the simulated total Na from a constant source rate model as described in the previous section. This constant rate model suggests that, while a part of the brightness variation in UVS data ( $\sim 20\%$  over a month) appears to be geometry driven (e.g., varying spacecraft and tangent point altitudes), as a rule the UVS Na response differs markedly from the model, indicating a true change in source rate over this period. Our results are in agreement with the independent methods of Colaprete et al. (2016), who found a factor of two variation in the Na levels near noon during the same 2014 February–March lunation period, with a Na maximum after full moon, and a minimum a few days past new moon. Note that Colaprete et al. (2016) did not consider the possibility that some of the observed Na variation can be attributed to scattering inside the telescope, but our consideration of this effect does not significantly alter the derived trend. Additionally, the Na

column densities are consistent with the results from Potter & Morgan (1998), and Killen et al. (2021).

The day-to-day variability over the course of the lunation presented in each panel could be associated with changes in the solar wind or meteoroid environment, but could also indicate Na inhomogeneity on the surface. In theory, the exposure of the lunar dayside to a changing solar wind environment should cause instantaneous changes seen across all local times. This appears to be the case in the LADEE observations and can be readily seen when the Moon transitions from the solar wind to Earth’s magnetosheath (densest) and magnetosphere (most rarefied) plasma conditions. Here the data shows clear Na enhancements once the Moon is within the magnetosheath regions, previously interpreted as due to the increased ion-enhanced diffusion rates (e.g., Sarantos et al. 2010).

While some of the observed variability appears to be attributed to solar wind variability, the day-to-day variation may also indicate nonuniformity of surficial Na and its vaporization parameters. To search for possible compositional enhancements, Figure 13 presents the wing continuum levels (panel (a)), along with the total (panel (b)) and residual Na emission (panel (c)) fixed in selenographic longitude coordinates for six local times. The black line comprises a smoothed fit to the residuals from these six local times (centered to remove the trend with local time seen in Figure 11). This smooth fit indicates a somewhat nonuniform Na exosphere with selenographic location, with slight enhancements over Mare regions, and broader depletions over the predominantly highland areas, in general agreement with that found by

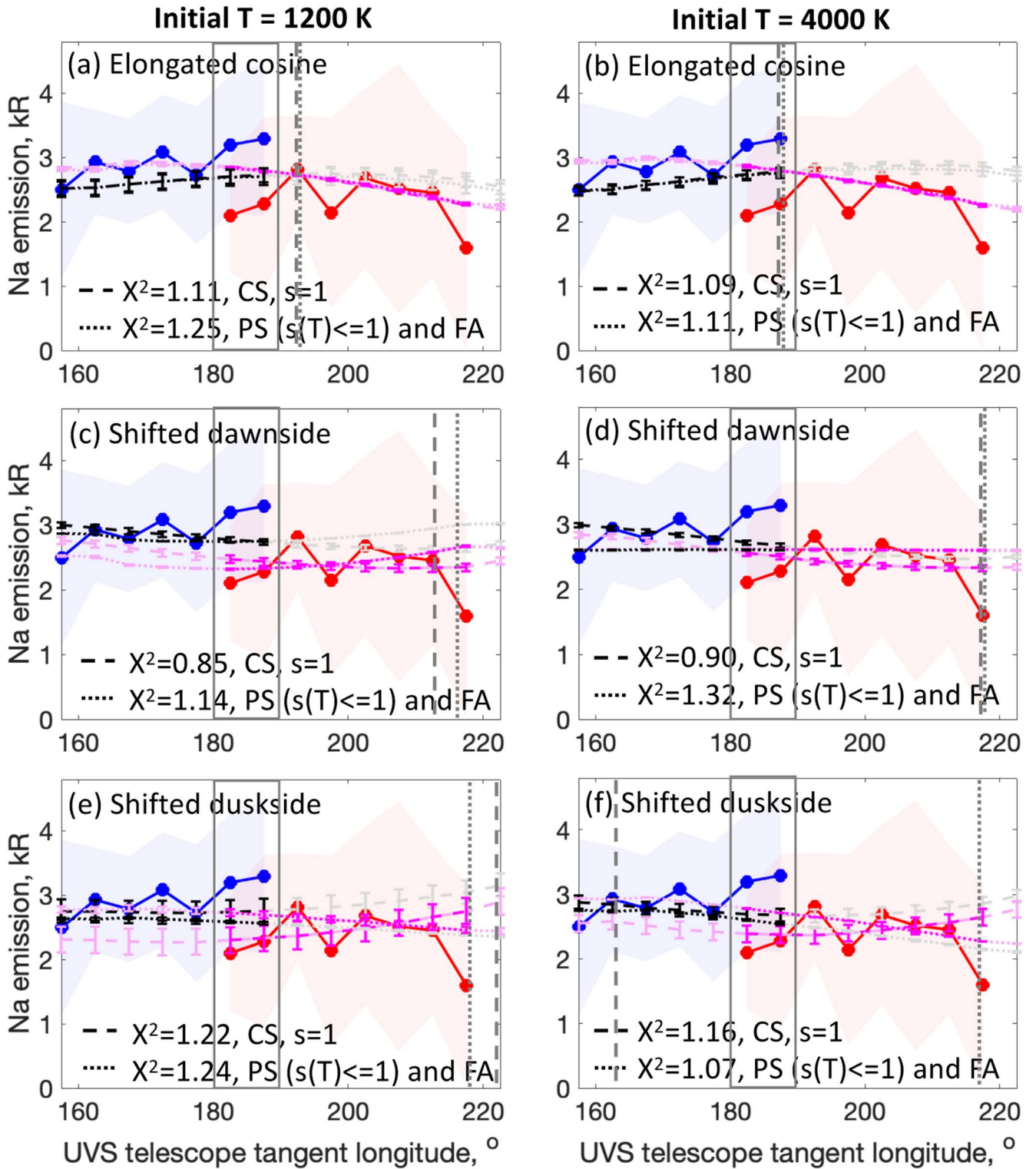


**Figure 10.** Comparison of different model simulations with the UVS data. Panels (a)–(b), (c)–(d), (e)–(f) correspond to an elongated cosine, the same model with the peak shifted  $20^\circ$  toward dawn, and then shifted  $20^\circ$  toward dusk, respectively. Panels (a), (c), and (e) have an initial source  $T = 1200$  K, while (b), (d), and (f) correspond to an initial source  $T = 4000$  K. Model simulations using backward-viewing limb geometry are in black, while magenta correspond to simulations with forward-viewing geometry. The dashed and dotted lines correspond to models with complete sticking, or  $s = 1$  (“CS,  $s = 1$ ”), and partial sticking ( $s(T) <= 1$ ) and full accommodation (“PS ( $s(T) <= 1$ ) and FA”), respectively. The chi-squared value for each pair of model lines (pair consists of either the dotted or the dashed backward and forward set) as compared to the UVS data is presented in the lower left corner of each panel.

Colaprete et al. (2016, their Figure 3(A)). The slight excess found over Mare soils is encouraging because it disqualifies the possibility that the trend of Figure 10 is driven by residual scattering in the telescope (the scattering is clearly expected to

be lower over dark Mare soils). However, it is worth noting that this enhancement over Mare regions may be consistent with the fact that the emission is more easily extracted from the continuum for lower albedo surfaces. We note that the Na

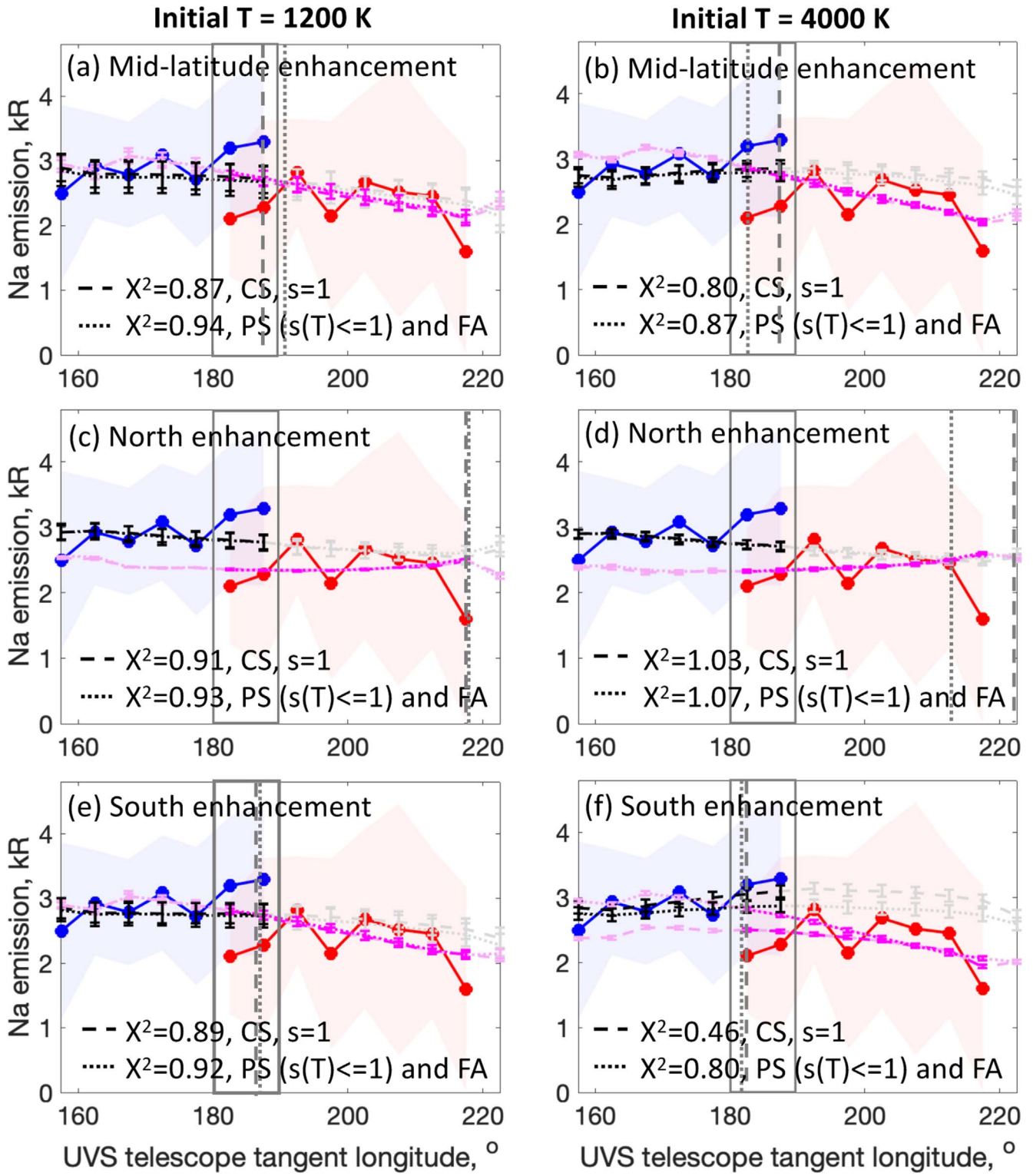


**Figure 11.** Comparison of different model simulations with the UVS data. Panels (a)–(b), (c)–(d), (e)–(f) correspond to a north–south midlatitude source with equatorial depletion, a source located in the north, and a source located in the south, respectively. Panels (a), (c), and (e) have an initial source  $T = 1200$  K, while (b), (d), and (f) correspond to an initial source  $T = 4000$  K. Model simulations using backward-viewing limb geometry are in black, while magenta correspond to simulations with forward-viewing geometry. The dashed and dotted lines correspond to models with complete sticking, or  $s = 1$  (“CS,  $s = 1$ ”), and partial sticking ( $s(T) <= 1$ ) and full accommodation (“PS ( $s(T) <= 1$ ) and FA”), respectively. The chi-squared value for each pair of model lines (pair consists of either the dotted or the dashed backward and forward set) as compared to the UVS data is presented in the lower left corner of each panel.

emission between  $-20^\circ$  and  $-40^\circ$  selenographic longitude (panel (c)) corresponds to where the continuum levels are at their lowest and is thus deemed to represent some of the *cleanest* data. This data is also shown in Figure 7 (panel (a)),

and the local time variation seen across the data set is clearly presented increasing confidence that the trends presented here are real. The residuals can be interpreted as a more accurate indicator of how the total content of the exosphere varies with

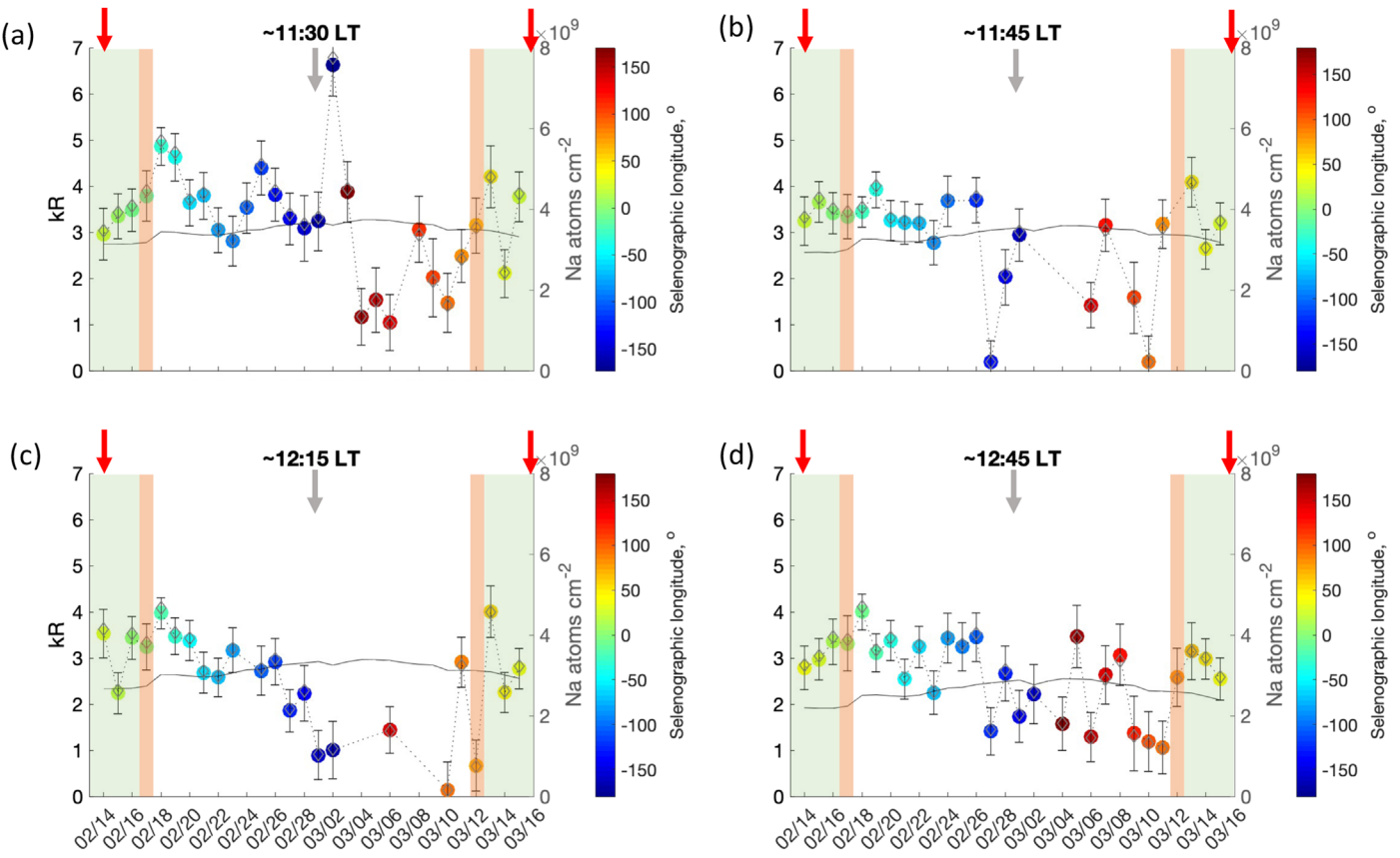


**Figure 12.** Total Na emission for four different local time (LT) bins for (a) 11:30 LT, (b) 11:45 LT, (c) 12:15 LT, and (d) 12:45 LT, with corresponding uncertainties (vertical bars). The black solid curves represent a second-order polynomial fit to the UVS data. The colored points correspond to the median selenographic longitude of the UVS telescope grazing point. Data consist of backward-viewing limb measurements only. The light gray line represents the simulated Na from a constant source rate model. The gray diamonds correspond to measured total UVS Na column density (right-hand-side y-axis). The red arrows indicate full moon, while the gray arrow indicates new moon phase. The shaded green and orange regions indicate when the Moon was within the Earth’s magnetotail and magnesheath regions.

the lunar phase more than the time series from one local time. While the lunar surface distribution of Na is currently unknown, it is possible that the variation in our UVS Na reflects the compositional changes in lunar soils, and/or is associated with varying lunar rock and grain sizes that may enhance or inhibit the desorption rate.

#### 4. Conclusions

In this work, we derived lunar exospheric Na emission from the NASA LADEE/UVS instrument over one full lunation, 2014 February–March, producing the first study of near-instantaneous variation of exospheric Na across the lunar dayside. Understanding the spatial and temporal variation of exospheric Na provides an opportunity to better understand the nature of surface boundary exospheres, which are found among many other bodies within our solar system.

Absolute Na emission and column abundance from this work are consistent with those inferred by ground-based observations. We found that, due to the limited viewing geometry and sensitivity of the instrument to scattering from the bright lunar surface, it is difficult to separate the latitudinal and local time contributions to the distribution of Na. Model simulations with a  $T = 4000$  K and a southern enhancement, and to a lesser extent a midlatitude enhancement and equatorial depletion, represent the best (but nonunique) fits to the UVS data within the corresponding uncertainties. Due to increased scattering as the telescope observed areas downwards of the subsolar point,

and through the comparison with models with dawnside or duskside source offsets, no evidence of a dawn–dusk asymmetry surrounding the subsolar region was obtained. It should be noted that, if the atmosphere is mainly provided by energetic processes (as indicated by our UVS-model comparisons), finding pronounced asymmetries would be difficult as the particles will have a high ballistic range.

We also quantified how the Na content varies with the lunar phase and found evidence of enhancements over the Mare regions. Although we acknowledge that this enhancement over Mare regions may be consistent with the fact that the emission is more easily extracted from the continuum for low albedo surfaces, the local time trends seen in the *cleanest* data above Mare regions increase the confidence in our findings. Day-to-day variability can be seen in the data set, and this could be caused by a number of factors including solar wind variability, the presence of currently undetected weak meteoroid showers, changes in the selenographic distribution of Na, and changes in gas–surface interaction parameters at different soils, as indicated by studies including Colaprete et al. (2016), Killen et al. (2021), Szalay et al. (2016), and Morrissey et al. (2022). Our time series of exospheric measurements will enable quantitative correlations of the exosphere with measurements of the solar wind environment at the Moon by the Acceleration, Reconnection, Turbulence and Electrodynamics of the Moon’s Interaction with the Sun spacecraft.

The extended coverage of local times provided with this analysis should be compared to exosphere models to accurately

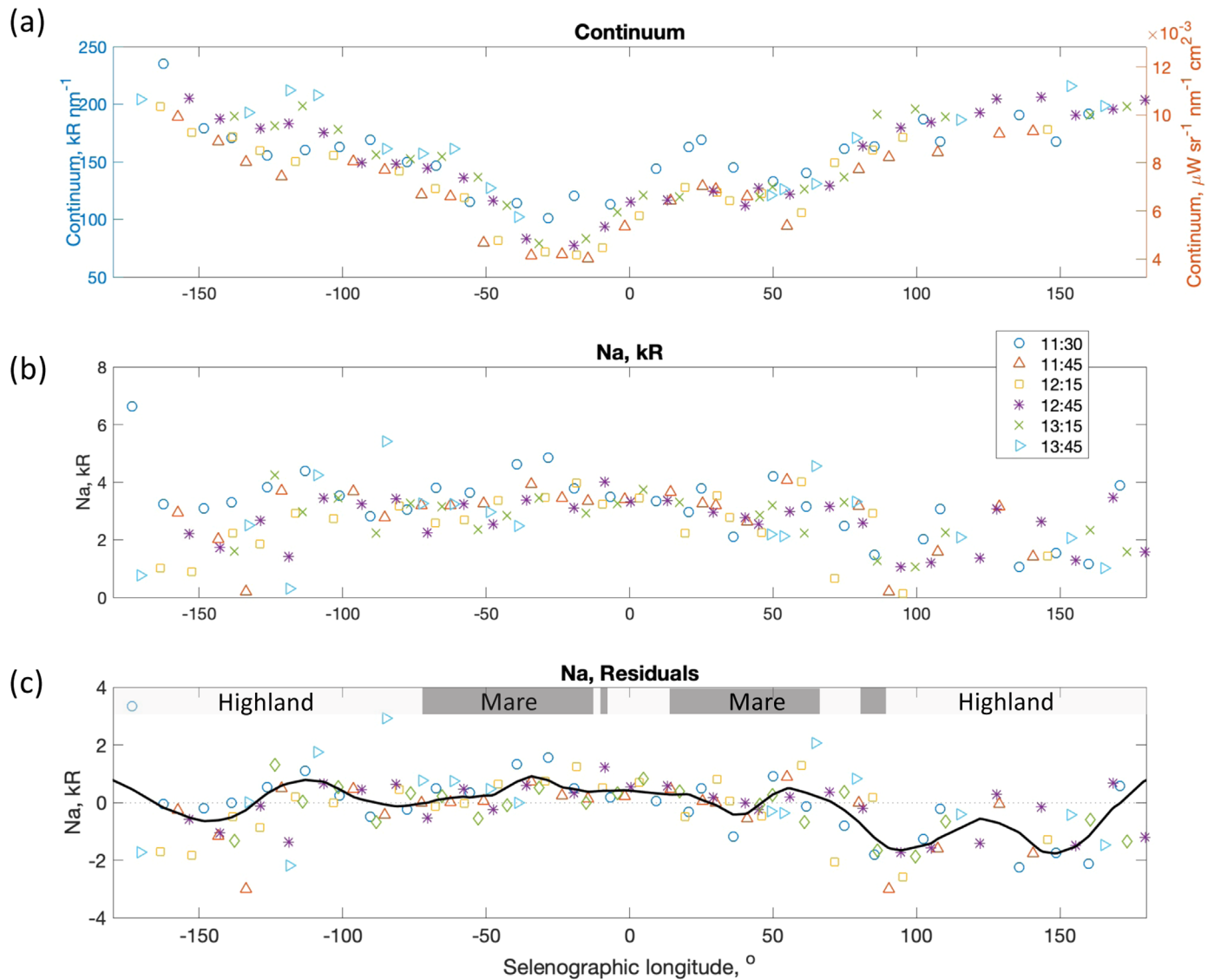


**Figure 13.** Total Na emission for six different local time bins as a function of selenographic longitude of the UVS telescope grazing point (panel (b)). Panel (c) shows the corresponding residual kR after normalizing with the median for the respective local time bin. The black solid line represents a 10% robust Loess smooth to the residual data. Highland (light gray) and mare (dark gray) areas are indicated by the shaded regions. Panel (c) shows the wing continuum levels as a function of selenographic longitude.

understand the global structure of the exosphere. In addition, the synergistic use of models and these measurements can be used to better understand the generation mechanisms of the Na exosphere, and to reevaluate the escape from the Moon, including a refinement of speed distributions of these gases through line width modeling (Kurupparatchi et al. 2018). Finally, we plan to extend our processing techniques to the full LADEE/UVS data set covering all five lunations. The remaining months of LADEE measurements can help establish whether a dawn–dusk asymmetry is observed in the Na exosphere during other lunations, which include major meteoroid showers, as well as assess the short-term response of the lunar exosphere to other episodic phenomena, such as coronal mass ejections.

E.C.M.D., M.S., and D.J. were supported through the NASA LDAP and ISFM programs. M.S. was also supported by the NASA Solar System Exploration Research Virtual Institute (SSERVI). E.M. was partially supported by NASA award NNX15AR04G to ERAU. This work uses publicly available

LADEE/UVS limb measurements, which can be found in the NASA Planetary Data System (PDS) at [https://pds-atmospheres.nmsu.edu/data\\_and\\_services/atmospheres\\_data/LADEE/uvss.html](https://pds-atmospheres.nmsu.edu/data_and_services/atmospheres_data/LADEE/uvss.html). We would also like to thank the anonymous reviewers for their diligence in reviewing the manuscript.

#### ORCID iDs

- E. C. M. Dawkins <https://orcid.org/0000-0001-6083-0725>
- M. Sarantos <https://orcid.org/0000-0003-0728-2971>
- D. Janches <https://orcid.org/0000-0001-8615-5166>
- E. Mierkiewicz <https://orcid.org/0000-0002-4283-3751>
- A. Colaprete <https://orcid.org/0000-0002-5847-2241>

#### References

- Athiray, P. S., Narendranath, S., Sreekumar, P., & Grande, M. 2014, *P&SS*, **104**, 279
- Bennett, C. J., McLain, J. L., Sarantos, M., et al. 2016, *JGRE*, **121**, 137
- Clark, R. N., & Roush, T. L. 1984, *JGR*, **89**, 6329

- Colaprete, A., Sarantos, M., Wooden, D. H., et al. 2016, *Sci*, **351**, 249
- Colaprete, A., Vargo, K., Shirley, M., et al. 2014, *SSRV*, **185**, 63
- Collier, M. R., Snowden, S. L., Sarantos, M., et al. 2014, *JGRE*, **119**, 1459
- Elphic, R. C., Delory, G. T., Hine, B. P., et al. 2015, in The Lunar Atmosphere and Dust Environment Explorer Mission (LADEE), ed. R. Elphic & C. Russell (Cham: Springer), 3
- Flynn, B., & Mendillo, M. 1993, *Sci*, **261**, 184
- Janches, D., Pokorný, P., Sarantos, M., et al. 2018, *GeoRL*, **45**, 1,713
- Kagitani, M., Taguchi, M., Yamazaki, A., et al. 2009, *EP&S*, **61**, 1025
- Kagitani, M., Taguchi, M., Yamazaki, A., et al. 2010, *PSS*, **58**, 1660
- Killen, R. M., Morgan, T. H., Potter, A. E., et al. 2019, *Icar*, **328**, 152
- Killen, R. M., Morgan, T. H., Potter, A. E., et al. 2021, *Icar*, **355**, 114155
- Kuruppuaratchi, D. C. P., Mierkiewicz, E. J., Oliversen, R. J., et al. 2018, *JGRE*, **123**, 2430
- LeBlanc, F., & Johnson, R. E. 2003, *Icar*, **162**, 261
- Mendillo, M., & Baumgardner, J. 1995, *Natur*, **377**, 404
- Morrisey, L. S., Tucker, O. J., Killen, R. M., Nakhla, S., & Savin, D. W. 2022, *ApJL*, **925**, L6
- Pokorný, P., Janches, D., Sarantos, M., et al. 2019, *JGR*, **124**, 752
- Potter, A. E., Killen, R. M., & Morgan, T. H. 2000, *JGR*, **105**, 15073
- Potter, A. E., & Morgan, T. H. 1988a, *Sci*, **241**, 675
- Potter, A. E., & Morgan, T. H. 1988b, *GeoRL*, **15**, 1515
- Potter, A. E., Jr., & Morgan, T. H. 1991, *GeoRL*, **18**, 2089
- Potter, A. E., & Morgan, T. H. 1998, *JGR*, **103**, 8581
- Sarantos, M., & Tsavachidis, S. 2020, *GeoRL*, **47**, e88930
- Savitzky, A., & Golay, M. J. E. 1964, *AnaCh*, **36**, 1627
- Sprague, A. L., Kozlowski, R. W. H., Hunten, D. M., Wells, W. K., & Grosse, F.A. 1992, *Icar*, **96**, 27
- Sprague, A. L., Sarantos, M., Hunten, D. M., Hill, R. E., & Kozlowski, R. W. H. 2012, *CaPh*, **90**, 725
- Stern, S. A. 1999, *RvGeo*, **37**, 453
- Szalay, J. R., Horányi, M., Colaprete, A., & Sarantos, M. 2016, *GeoRL*, **43**, 6096
- Tyler, A. L., Kozlowski, R. W. H., & Hunten, D. M. 1988, *GeoRL*, **15**, 1141
- Yakshinskiy, B. Y., & Madey, J. E. 1999, *Natur*, **400**, 642
- Yokota, S., Tanaka, T., Saito, Y., et al. 2014, *JGRE*, **119**, 798
- Wang, Y. C., & Ip, W. H. 2011, *Icar*, **216**, 387
- Wooden, D. H., Cook, A. M., Colaprete, A., et al. 2016, *NatGe*, **9**, 665